

DATA STORAGE

Three-dimensional supercritical resolved light-induced magnetic holography

Chenglong Hao,^{1,2} Zhongquan Nie,³ Huapeng Ye,¹ Hao Li,² Yang Luo,¹ Rui Feng,¹ Xia Yu,² Feng Wen,^{1,4} Ying Zhang,² Changyuan Yu,^{1,5} Jinghua Teng,⁶ Boris Luk'yanchuk,^{7,8,9} Cheng-Wei Qiu^{1,10*}

In the era of big data, there exists a growing gap between data generated and storage capacity using two-dimensional (2D) magnetic storage technologies (for example, hard disk drives), because they have reached their performance saturation. 3D volumetric all-optical magnetic holography is emerging rapidly as a promising road map to realizing high-density capacity for its fast magnetization control and subwavelength magnetization volume. However, most of the reported light-induced magnetization confronts the problems of impurely longitudinal magnetization, diffraction-limited spot, and uncontrollable magnetization reversal. To overcome these challenges, we propose a novel 3D light-induced magnetic holography based on the conceptual supercritical design with multibeam combination in the 4π microscopic system. We theoretically demonstrate a 3D deep super-resolved ($\sim\lambda^3/59$) purely longitudinal magnetization spot by focusing six coherent circularly polarized beams with two opposing high numerical aperture objectives, which allows 3D magnetic holography with a volumetric storage density of up to 1872 terabit per cubic inches. The number and locations of the super-resolved magnetization spots are controllable, and thus, desired magnetization arrays in 3D volume can be produced with properly designed phase filters. Moreover, flexible magnetization reversals are also demonstrated in multifocal arrays by using different illuminations with opposite light helicity. In addition to data storage, this magnetic holography may find applications in information security, such as identity verification for a credit card with magnetic stripe.

INTRODUCTION

The demand for data storage has grown rapidly over the past several decades. Tremendous progress has been made in increasing the areal density—the number of bits per unit area formed on the magnetic material surface (1–10). However, because of the superparamagnetic limit (1), the areal density of longitudinal magnetic recording and perpendicular magnetic recording techniques is restricted to 100 Gbit/in² (2, 3) and 1 Tbit/in² (4), respectively. The areal density can be further increased by adopting novel recording and patterning methods, such as heat-assisted magnetic recording (6, 7) and bit-patterned media (8, 9) where the hybrid recording head and patterned magnetic grains are used. Moreover, if both of the aforementioned techniques are combined together, then the areal density can be remarkably enhanced to 10 Tbit/in² (10). However, the areal density improvement is eventually limited by the attainable fabrication accuracy (11) because the conventional magnetic-based data storage technique relies on recording the data merely on the two-dimensional (2D) material surface, such as the hard disk drive (HDD).

3D magnetic recording (volumetric magnetic hologram) is an alternative strategy to realize extremely high-density magnetic storage (12–16). In principle, a conventional magnetic hologram is written by so-called “thermomagnetic recording.” Volumetric magnetic holograms by thermomagnetic writing have also been demonstrated (16). It has been shown that the information can be retained in the magnetic film and then successfully reconstructed from the 3D hologram even though the recording locations are overlapping (16). However, all of the aforementioned magnetic holograms that depend entirely on the thermal origin suffer from poor recording density and slow magnetization reversal, which is on the order of 100 ps (17).

Opto-magnetism, which is a nonthermal effect of light on magnetic materials, provides subpicosecond-level magnetization control (18). Therefore, opto-magnetism emerges rapidly as a powerful pathway for fast magnetization control of light in magneto-optical (MO) materials. Opto-magnetism also provides an approach for accessing sub-wavelength magnetization volume all-optically, which sheds light on the realization of 3D all-optical magnetic recording (AOMR) (18–20). The AOMR is first experimentally demonstrated in the GdFeCo alloys by circularly polarized light with opposite helicity (18). The low numerical aperture (NA) [~ 0.04 at a wavelength (λ) of 800 nm] of the focusing lens in the AOMR system leads to quasi-longitudinal magnetization and relatively large laser size, which defines a switched domain with a diameter of 10 μm (18). Theoretically, the longitudinal magnetization is four orders of magnitude larger than the transverse magnetization (21). However, although all-optical helicity-dependent magnetic switching for magnetic recording has been demonstrated with longitudinal magnetization, so far several crucial problems have thwarted the realization of 3D AOMR. First, the polarization orientation of the triggered magnetization tends to be intricate rather than purely longitudinally polarized within the effective magnetization domain. The impurity of the induced magnetization conversely hinders the availability of high-efficiency

¹Department of Electrical and Computer Engineering, National University of Singapore, 4 Engineering Drive 3, Singapore 117583, Singapore. ²Singapore Institute of Manufacturing Technology, A*STAR (Agency for Science, Technology and Research), 2 Fusionopolis Way, Kinesis, Singapore 138634, Singapore. ³Key Laboratory of Advanced Transducers and Intelligent Control System, Ministry of Education and Shanxi Province, College of Physics and Optoelectronics, Taiyuan University of Technology, Taiyuan 030024, China. ⁴Key Laboratory for Physical Electronics and Devices of the Ministry of Education and Institute of Wide Bandgap Semiconductors, Xi'an Jiaotong University, Xi'an 710049, China. ⁵Department of Electronic and Information Engineering, The Hong Kong Polytechnic University, Hung Hom, Kowloon, Hong Kong. ⁶Institute of Materials Research and Engineering, A*STAR, 2 Fusionopolis Way, Innovis, Singapore 138634, Singapore. ⁷Data Storage Institute, A*STAR, Singapore 138634, Singapore. ⁸Division of Physics and Applied Physics, School of Physical and Mathematical Sciences, Nanyang Technological University, Singapore 637371, Singapore. ⁹Faculty of Physics, Lomonosov Moscow State University, Moscow 119991, Russia. ¹⁰SZU-NUS Collaborative Innovation Center for Optoelectronic Science and Technology, Shenzhen University, Shenzhen 518060, People's Republic of China.

*Corresponding author. Email: eleq@nus.edu.sg

AOMR (18–22). Studies on enhancing the purity of the longitudinal component in the magnetization zone are done via inverse Faraday effect (23–25); however, the realization of purely longitudinal magnetization is still challenging. Second, 3D deep-subwavelength magnetization volume far beyond the diffraction limit ($\sim\lambda^3/8$) allows ultrahigh-density magnetic data storage. Nevertheless, there is a growing gap between the requirements of the cutting-edge MO devices and the achievable resolution in a 3D volume. A 4π high-NA focusing system and two counterpropagating radially polarized hollow Gaussian vortex beams have produced a subwavelength magnetization spot (MS) (26). However, although the 4π focusing configuration improves the longitudinal size of the magnetic spot by four to seven times, the lateral size is still diffraction-limited. Moreover, because of the constructive interference of the longitudinal electric field components, this strategy suffers from strong side lobes, rendering it less attractive in ultrahigh-density magnetic recording. Finally, as one of the most important processes linked to MO data recording, single-spot magnetization reversal can be obtained by circularly polarized light (18). However, flexible magnetization reversal with multiple MSs, which will greatly increase the recording throughput by parallel magnetization, has not yet been demonstrated. Generally, the aforementioned challenges constitute the fundamental barriers to the development of 3D MO data recording technology.

In this regard, we propose a novel road map for all-optical magnetic holography based on the supercritical design and beam combination. We theoretically demonstrate volumetric magnetic holography with a super-resolved ($\sim\lambda^3/59$) purely longitudinal MS, under the illumination of circularly polarized light. Such a high-resolution MS is achieved with a lateral size of 0.3566λ without significant side lobes and stably maintains a longitudinal size of 0.2550λ with moderate side lobes ($<30\%$). By judiciously manipulating the phase of incident beams, we can construct arbitrary arrays of 3D super-resolved MSs with almost perfect uniformity. Moreover, the magnetization reversal can also be realized by changing the helicity of incident waves (from left-handed circularly polarized beams to right-handed circularly polarized beams and vice versa). Our results pave the way for developing 3D ultrahigh-density AOMR. In addition to data recording, this 3D magnetic holography may also find applications in information security.

RESULTS

Generation of 3D supercritical resolved MS in all-optical magnetic holography

The magnetization induced by the lateral supercritical light spot is shown in Fig. 1. The overall magnetization distribution of the spot is plotted in Fig. 1A. The lateral full width at half maximum (FWHM) of MS is 0.3566λ , whereas the diffraction limit spot size is 0.4255λ . In the meantime, the axial FWHM of MS is 0.255λ , which is enormously suppressed by the 4π system. The side-lobe intensity is greatly suppressed below 0.3 (normalized intensity) by beam combination. Therefore, the 3D deep super-resolved voxel of approximately $\lambda^3/59$ is achieved, which is far smaller than the diffraction limit of $\lambda^3/8$. The magnetization components along the lateral white dashed line are shown in Fig. 1B. The radial magnetization component (M_r) vanishes completely, and the maximum of the azimuthal magnetization component (M_ϕ) is estimated to be $\sim 30\%$ of the axial magnetization component (M_z), leading to a purely longitudinal magnetization. Figure 1C shows the axial magnetization components along the axial white dashed line in Fig. 1A. Both M_r and M_ϕ disappear along the axial direc-

tion, leading to a purely longitudinal magnetization, which is determined by M_z . The intensity of the axial side lobes is estimated to be approximately 30% of the central spot, which distinguishes the current approach from the 4π configuration working with strongly focused cylindrically polarized vortex beams, where the reported side-lobe intensity is much larger than 50% (17). To better illustrate the property of the MS, the 3D slices of MS are shown in Fig. 1D. Five layers of the XY planes are equally placed between $-\lambda$ and $+\lambda$ with an identical interval of 0.5λ along the z axis. The maximum side lobes are located at $Z = \pm 0.5\lambda$ with an intensity of $\sim 30\%$.

For 3D magnetic recording, the theoretical storage density limit is mainly determined by the volume of the MS. Theoretically, with the volumetric super-resolved voxel (approximately $\lambda^3/59$), a storage density of $1/59 \lambda^{-3}$, that is, 1872 Tbit/in^3 at $\lambda = 800 \text{ nm}$, should be attainable. This remarkable result is two orders better than the state-of-the-art HDD, solid-state disk, and linear tape based on sophisticated nanofabrication technology in terms of volumetric storage density (11). It should also be noted that this volumetric storage density is one order of magnitude higher than the optimistic trend prediction in the year 2025 (11).

In addition to recording density, the long-term stability is also of vital importance in magnetic recording. The MO material thermal stability factor $K_u V/kT$ must exceed 60 to ensure information stability after 10 years of archiving in magnetic recording media (27), where K_u , V , k , and T are the anisotropy constant of the MO material, the volume of MS, the Boltzmann constant, and the temperature, respectively. The anisotropy constant of the GdFeCo alloy is approximately $3 \times 10^{-2} \text{ J/cm}^3$ (28, 29). The calculated stability factor is approximately 6.288×10^4 with achieved super-resolved MS (approximately $\lambda^3/59$) and room temperature at 300 K. Therefore, the GdFeCo alloy is a good candidate for long-term data recording.

Creation of 3D lateral supercritical longitudinal magnetization arrays in magnetic holography

It is of vital importance that the 3D super-resolved longitudinal MSs can be created in arrays with arbitrarily controlled spot locations and numbers, which could greatly help to increase the throughput of the data recording. The principle of the current approach to generating multifocal arrays is to iteratively optimize the phase modulation at the back aperture of the objective so that the desired arrays can be achieved in the focal region (30, 31). However, it should be noted that this iterative approach is time-consuming and lacks physical insight. Hence, we propose and demonstrate an analytical method to generate the desired MS arrays by multiple phase filters (MPFs) (as shown in Fig. 2A). The theoretical model for the fast Fourier transform method is shown in the Supplementary Materials (see Theoretical model for multifoci by multiple phase filters). By adopting the fast Fourier transform method, the electric field distribution in the focal region is the convolution of the Fourier transform of the phase modulation and the Fourier transform of the incident electric field with uniform wavefront. Therefore, the phase function of the MPFs can be calculated analytically as

$$t(x, y) = \sum_{i=1}^N \exp[-ik(a_i x + b_i y)] \times \exp(-ikc_i \cos\theta) \quad (1)$$

where N is an integer, giving the total number of spots along the x , y , and z directions; a_i , b_i , and c_i represent the displacements along the x , y , and z directions, respectively; and k is the wave number. Therefore, the phase function is a superposition of the electric fields of each spot at the back aperture.

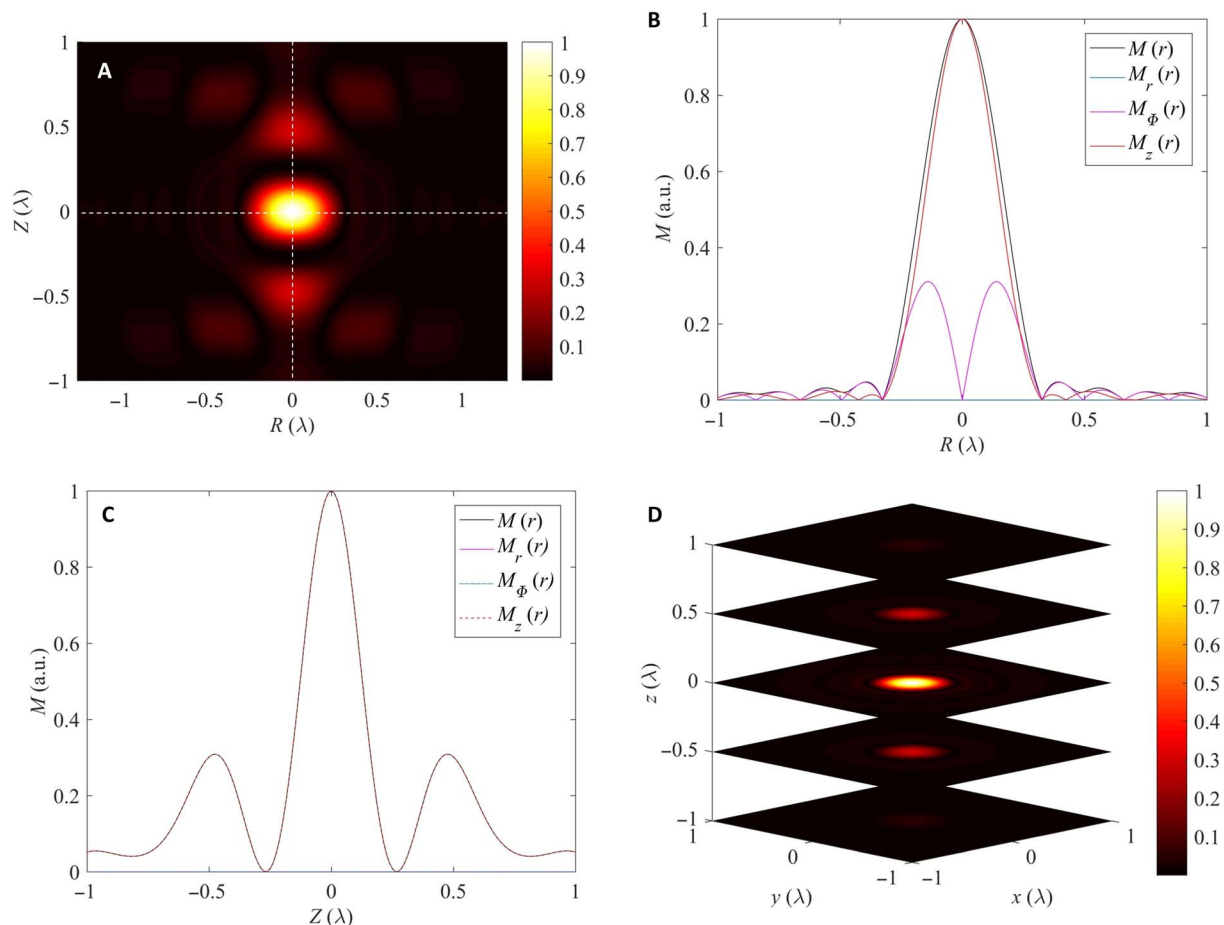


Fig. 1. Single 3D super-resolved longitudinal MS. (A) The overall magnetization distribution in the RZ plane. (B) Magnetization components in the lateral direction [horizontal white dashed line in (A)]. a.u., arbitrary units. (C) Magnetization components in the axial direction [vertical white dashed line in (A)]. (D) 3D slices of MS along the z axis.

Here, we demonstrate a “pyramid” spot pattern with the five MSs. The corresponding phase pattern is arranged periodically in the entire pupil plane, as shown in Fig. 2A, which contributes to shift the single MS to the appointed positions and, thus, form the pyramid. Figure 2B illustrates the schematic of the pyramidal pattern, with red spots representing the vertexes. The positions of these vertexes are $(4\lambda, 4\lambda, 0)$, $(4\lambda, -4\lambda, 0)$, $(-4\lambda, 4\lambda, 0)$, $(-4\lambda, -4\lambda, 0)$, and $(0, 0, 4\sqrt{2}\lambda)$. The cross-sectional maps of the 3D MS array in the $z = 0$ plane (plane ABCD) and the $x + y = 0$ plane (plane EGCA) are shown in Fig. 2 (C and D, respectively). It is revealed that the resolution of all the MSs is almost the same as that without undergoing the pyramidal MPFs. More specifically, the lateral FWHM of MS in the pyramid is estimated to be 0.37λ , comparable to 0.3566λ in the absence of MPFs, and the axial FWHM of MS in the pyramid is 0.252λ , comparable to 0.255λ in the absence of MPFs. Moreover, we also find that the magnetization direction of MSs in the array is almost purely longitudinal.

In addition to the spatial resolution and polarization, the uniformity of the magnetization amplitude is routinely used to evaluate the performance of the MS arrays. Traditionally, the uniformity is defined as $1 - D$, where D represents the maximum difference among all MSs in the normalized magnetization distribution. The uniformities in plane ABCD and plane EGCA are evaluated as 100 and 96.9%, respectively. Such a high uniformity can offer an excellent tolerance in multifocal off-axis MO recording and maintain high accuracy in multifocal magnetic

resonance imaging. Compared with a light-triggered magnetization chain, which increasingly weakens from the geometric focus (32), the reported MS array in this study is more uniform. In addition to the uniformity, the universal applicability of this model is also remarkable. This is explicitly shown by the example in fig. S2, where a complex geometry [the logo of National University of Singapore (NUS)] is adopted. The NUS logo is formed by multiple off-axis and off-focus MSs. The letters “N,” “U,” and “S” are located at $z = 8\lambda, 0$, and -8λ with 10, 10, and 11 MSs, respectively.

Arbitrary magnetization reversal in MS array via different illuminations

In magnetic memory devices, logical bits (“ones” and “zeros”) are stored by setting the magnetization vector of the individual magnetic domains either “up” or “down.” Thus, the recording of one bit corresponds to magnetization reversal. All-optical magnetization reversal has been realized by engineered material combinations (20) and circularly polarized light (18). However, as one of the most important processes linked to MO data storage, arbitrary magnetization reversal in MS arrays has not yet been demonstrated. Here, we attempt to demonstrate numerically arbitrary magnetization reversal in the pyramid.

The magnetization direction can be controlled by the helicity of the incident light. Here, the magnetization reversal is achieved via two

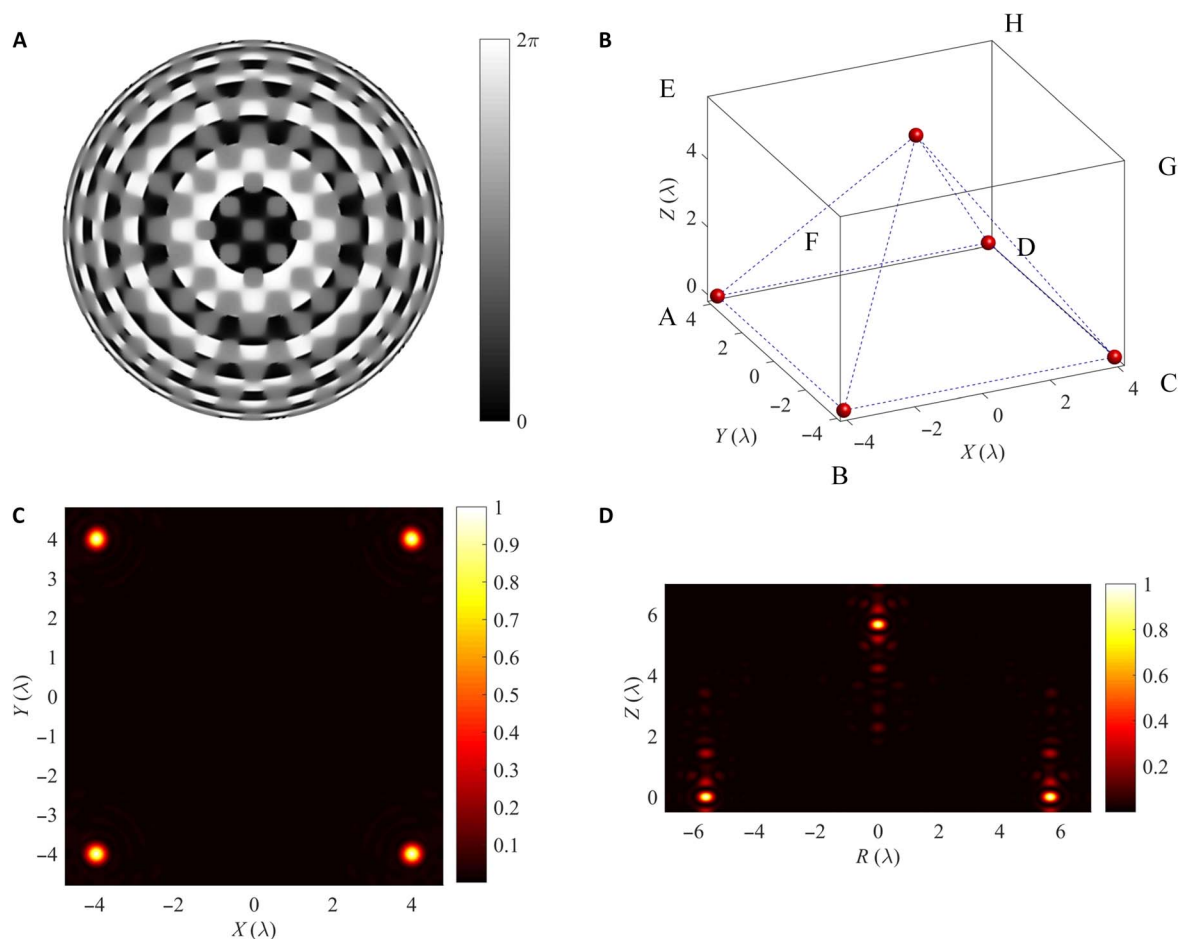


Fig. 2. The 3D super-resolved pyramidal MS array in the magnetic hologram. (A) The phase pattern of MPSs for the pyramidal pattern. (B) The 3D spatial pyramid MS arrangement. (C) The cross-sectional map of 3D MS array in the plane ABCD. (D) The cross-sectional map of 3D MS array in the plane EGCA.

illuminations with opposite light helicity. The theoretical validation of the magnetization reversal by different light helicity is demonstrated in the Supplementary Materials (see Theory of light induced magnetization and magnetization reversal with eqs. S16 and S17). Figure 3 illustrates one- and three-MS magnetization reversal in the pyramid. The schematic of one-spot (peak of the pyramid) magnetization reversal is shown in Fig. 3A. Four 3D super-resolved spots with positive magnetization are generated by the first illumination with left-handed circular polarization. These MSs are indicated with red spots with positive z arrows in Fig. 3A. The MS in plane EFGH is created by the second illumination with right-handed circular polarization. This MS is indicated with blue spots with negative z arrows representing its magnetization direction. The cross-sectional maps of the 3D MS array in the $z = 0$ plane (plane ABCD) and $x + y = 0$ (plane EGCA) are shown in Fig. 3 (B and C, respectively). As shown in Fig. 3C, the peak of the pyramid is perfectly reversed in its magnetization direction. The same principle can be used to realize the three-MS reversal, and it is demonstrated in Fig. 3 (D to F). Figure 3D shows the schematic of the three-MS reversal. The reversed MSs are indicated by blue spots with negative z arrows. Figure 3 (E and F) shows the cross-sectional maps of MSs in plane ABCD and plane EGCA, respectively. It should be emphasized that the resolution and uniformity in both magnetization reversal cases are the same as that without magnetization reversal.

Identity verification

In addition to data recording, this 3D magnetic holography could also find applications in information security, for example, identity verification for a credit card. Currently, the payment with credit cards is basically reading the information from the magnetic stripe. The main drawback of the conventional magnetic stripe is that it is not difficult to counterfeit technically. A new dimension of security could be achieved by adding this all-optical magnetic holography to the conventional magnetic stripe. The prototype of this novel routine is briefly illustrated in Fig. 4, where the QR codes of the NUS website link and logo are recorded in the same layer with logic bits “1” and “0,” respectively. When the rotation-mounted polarizer is rotated to the position of the triangle, only logical bits “1” are captured by the charge-coupled device (CCD) camera, whereas the “0” is filtered. Hence, the QR code of the NUS website link is reconstructed. Similarly, the logo of NUS can be reconstructed by rotating the polarizer to the position of the hexagram. If the volumetric magnetic hologram can be integrated with the credit card, then the information, such as the signature of the credit card holder, could be regarded as the verification code during transactions. This 3D all-optical magnetic holography can help to avoid financial crime because the volumetric magnetic hologram is very difficult to forge due to the expensive, specialized, and technologically advanced equipment involved.

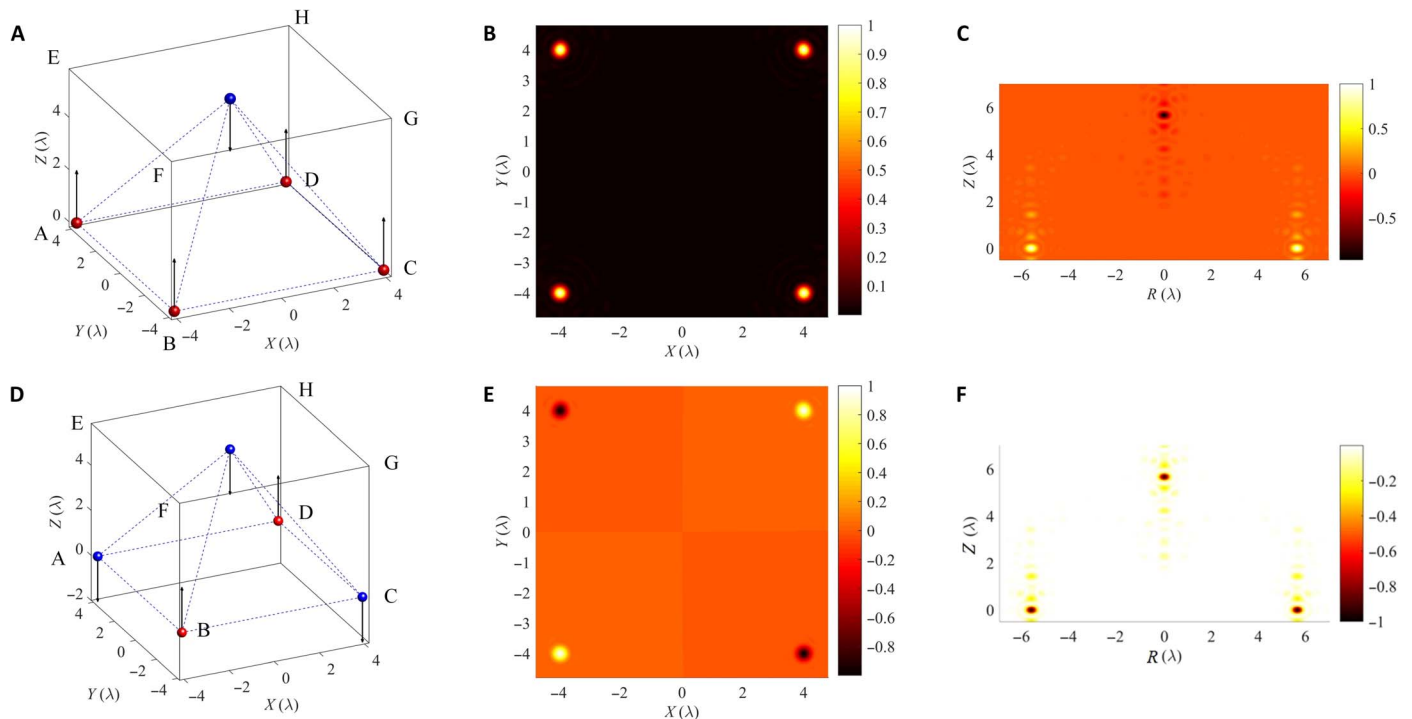


Fig. 3. The magnetization reversal in the pyramid. (A and D) Schematics of one-spot and three-spot reversal, with arrows indicating their respective magnetization directions. (B and E) The cross-sectional maps of 3D MS array in the plane ABCD after reversal. (C and F) The cross-sectional maps of 3D MS array in the plane EGCA after reversal.

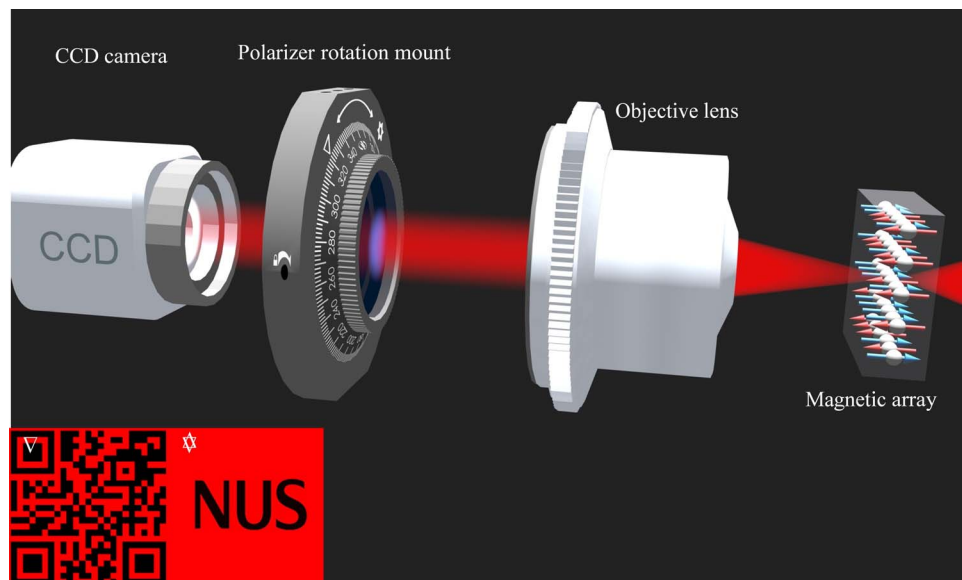


Fig. 4. Illustration for identity verification. The linearly polarized light is incident perpendicular to the magnetic hologram on the magnetic array. The QR codes of the NUS website and logo are recorded in the same layer with logic bits “1” and “0,” respectively. When the rotation-mounted polarizer is rotated to the position of the triangle, the QR code of the NUS website link is reconstructed. Similarly, the logo of NUS will be reconstructed by rotating the polarizer to the position of the hexagram.

DISCUSSION

In summary, we have theoretically demonstrated the light-induced magnetic holography by supercritical design and 4π beam combination microscopic system. The purely longitudinal magnetization is achieved

by destructive interference of the axial electric field through 4π configuration. On the basis of the supercritical design, a 3D deep-subwavelength ($\sim \lambda^3/59$) longitudinal MS with negligible lateral side lobes and moderate axial side lobes has been demonstrated for the first time, which potentially

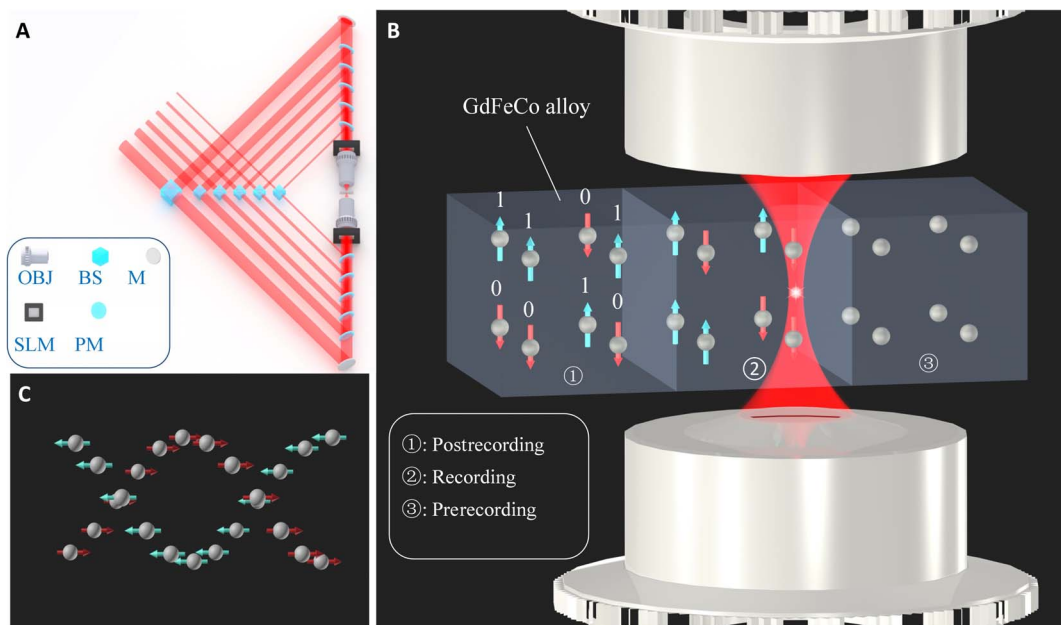


Fig. 5. Optical scheme for achieving super-resolved MS. (A) Schematic of the 4π beam combination microscopic system integrated with MPFs encoded by spatial light modulators (SLMs). The light wavelength is 800 nm. Six coherent beams are first combined and then focused to the magnetic hologram (an isotropic MO medium) located at the focal plane of the proposed system. OBJ, objective (oil-immersed lens; NA, 1.43); BS, beam splitter; PM, pellicle mirror; M, mirror. (B) The recording process of the magnetic hologram. The magnetic hologram is longitudinally magnetized because of the inverse Faraday effect. Zone ① is the postrecording zone, zone ② is the zone in recording process, and zone ③ is the zone prerecording. (C) Schematic of magnetization reversal. Positive MSs with blue arrows are induced by left-hand circularly polarized light, and negative MSs with red arrows are induced by right-hand circularly polarized light.

allows for 3D magnetic holography with a volumetric storage density as high as 1872 Tbit/in³. More significantly, arbitrary MS arrays, for example, the pyramidal 3D super-resolved longitudinal MS arrays, can be generated with optimized MPFs according to the locations and numbers of the MSs. Flexible magnetization reversal in a multifocal off-axis pattern has also been demonstrated by controlling the helicity of the incidence. Both the generated MSs and reversed MSs have excellent uniformities, making them an appealing platform for developing light-induced magnetic memory devices. From the experimental perspective, the possibility of achieving the powerful MS arrays with MPFs is particularly fascinating due to the application of dynamic SLM. Volumetric magnetic holography can be applied broadly in AOMR (18–20), confocal and magnetic resonance microscopy (33), and spintronic devices (34, 35). Moreover, volumetric magnetic holography can be applied to information security, for example, identity verification for a credit card with magnetic stripe.

Although the above results demonstrate potential applications, especially in AOMR, the complexity of the 4π beam combination microscopic system might be an issue in the experimental process. The 4π beam combination microscopic system involves challenging alignment, because multiple beams have to be precisely aligned. However, this is not unachievable. Coherent beam combining in fiber can be a potential way to implement this 4π beam combination design.

MATERIALS AND METHODS

Optical scheme for magnetic holography with supercritical deep-resolved MS

Essentially, the key to garner purely longitudinal magnetization all-optically in the magnetic hologram is to remove the electric field along

the axial direction (E_z). Multiple methods have been proposed to achieve destructive interference of E_z , such as focusing an azimuthally polarized vortex beam (36), amplitude/phase modulation using annular vortex binary optics (37, 38), and 4π microscopic system by counter-propagating two identically focused beams (26, 39–41). Among those methods, the 4π microscopic system is preferred because of its fascinating capability in simultaneously achieving axial super-resolution. However, it should be emphasized that the lateral resolution cannot be improved with the 4π microscopic system. Moreover, prominent side lobes with intensity up to 50% of the central peak intensity are inevitable, rendering this method less attractive in ultrahigh-density magnetic recording. Aiming to overcome these challenges, this study proposes a novel scheme based on a supercritical design by beam combination.

The supercritical design was implemented by conceptually developing a beam combination 4π microscopic system, as shown in Fig. 5A. Six coherent beams ($\lambda = 800$ nm) with identical polarization handedness were first modulated to the designed apertures (α_i) and amplitude coefficients (C_i) (table S1). These beams were divided into two groups by six beam splitters and then directed by mirrors toward two opposing high-NA objective lenses (NA, 1.43). Each group of beams passing through the SLMs was finally focused by the high-NA objectives. Without additional phase modulation from SLMs, only the axial magnetic component M_z with nonzero value existed in the focal region. Therefore, a single super-resolved purely longitudinal MS can be generated by these two groups of beams. The SLMs encoding the superposition of desired multiple off-focus and off-axis phase patterns were used as MPFs. By modulating the wavefronts of all beams with properly designed MPFs, arrays of 3D super-resolved purely longitudinal MSs can be created in the magnetic hologram, which is placed at the focal region perpendicular to the optical axis.

The vectorial electric field distributions in the focal region can be calculated using the Debye diffraction theory (eqs. S1 to S8). The interference of the focal fields of the two objectives is (42)

$$\mathbf{E}_t(r, \varphi, z) = \mathbf{E}(r, \varphi, z) + \mathbf{E}(r, \varphi, -z) \quad (2)$$

where $\mathbf{E}(r, \varphi, z)$ and $\mathbf{E}(r, \varphi, -z)$ stand for the electric fields of the up and down objectives, respectively, in Fig. 5A. The $\mathbf{E}(r, \varphi, \pm z)$ can be expressed as

$$\mathbf{E}(r, \varphi, \pm z) = \sum_{i=1}^6 C_i \mathbf{E}_i(r, \varphi, \pm z) \quad (3)$$

where $\mathbf{E}_i(r, \varphi, \pm z)$ stand for the electric fields of the sub-beam with aperture α_i . The detailed theoretical model of the beam combination method in 4π microscopy is given in the Supplementary Materials (see Theoretical model for 4π microscopy and beams combination method with eqs. S10 to S13). By properly optimizing the apertures of incident beams and their amplitude coefficients, the lateral resolution of the focal spot can be remarkably improved, and the side lobes in longitudinal direction can be greatly suppressed simultaneously. The optimization process is given in detail in the Supplementary Materials (see Optimization on lateral supercritical design and axial side lobes suppression).

The MO material was the GdFeCo alloy, which is widely used for all-optical magnetization (18–20). In magnetic memory devices, logical bits (“ones” and “zeros”) were stored by setting the magnetization vector of the individual magnetic domains either up or down. The process of magnetic holographic recording is shown in Fig. 5B. The magnets were magnetized up or down by the light stimulus according to the logical bits to be recorded. Zone ① is postrecording, where logic bits are indicated by “1” and “0.” The logic bits are in the process of recording in zone ②. Zone ③ is the zone that is prerecording. For the magnetic hologram in the focal region of the objective lenses, the conducting electrons can be regarded as collisionless plasma (43), which can migrate freely. The induced static magnetization in the magnetic hologram is the vector product of the electric field, which can be calculated as (25)

$$\mathbf{M}(r, \varphi, z) = i\gamma \mathbf{E}_t \times \mathbf{E}_t^* \quad (4)$$

where \mathbf{E}_t^* denotes the complex conjugate of \mathbf{E}_t , and γ is the MO susceptibility. The γ can be expressed as (43)

$$\gamma = \frac{\epsilon_0 e \omega_p^2}{4m\omega^3} \quad (5)$$

where ϵ_0 is the relative permittivity of vacuum, e is the electron charge, m is the electron mass, ω is frequency of electric field of light, and $\omega_p = (\langle n \rangle e^2 / m\epsilon_0)^{1/2}$ is the plasma frequency. The brackets $\langle \rangle$ denote the time average of the electron density n over several periods of the light electric field. A strong dependence of the magnetization generated by the inverse Faraday effect on the frequency of the applied light field $\mathbf{M} \propto \omega^{-3}$ is indicated in Eqs. 4 and 5. Although the MO susceptibility depends strongly on the frequency of light, the magnetizations in the magnetic hologram in different directions were determined by the vectorial electric field components polarizing along different directions. The details about the theoretical analysis of the light-induced

magnetization are shown in the Supplementary Materials (see Theory of light induced magnetization and magnetization reversal with eqs. S13, S16, and S17).

The magnetization reversal can be achieved by changing the polarization handedness of the incident light (18). Therefore, the flexible magnetization reversal can be implemented by different illuminations with opposite polarization handedness. The schematic of magnetization reversal is shown in Fig. 5C. The light-induced MSs form a double helix pattern in the focal region, as shown in Fig. 5C, where the blue arrows stand for positive magnetization and the red arrows stand for the negative ones. The formation of this double helix pattern consists of two illuminations. The first illumination forms the helix with positive magnetization. Then, the second illumination with opposite polarization handedness forms the negative one.

Supercritical criterion

The overall area of the MS in all-optical magnetic holography was determined by the size of the focal spot. It implies that the focal spot size should be further reduced if we want to achieve ultrahigh-density storage capacity. Generally, for the spherical lens-based optical imaging system, the lateral size of its focal spot was limited by $0.61\lambda/\text{NA}$ (above the diffraction limit), which is well known as the Rayleigh criterion (RC) (44). Subdiffraction focusing was feasible at the cost of the increasing side lobes. For unpolarized incident beams, light with higher spatial frequencies corresponded to a smaller main spot. The extreme case is that light with only the maximum spatial frequency can be focused into a hot spot with an intensity distribution similar to that of $|J_0(kr\text{NA})|^2$, which is termed as “maximum-frequency spot,” where $k = 2\pi/\lambda$ and λ is the wavelength (45, 46). For the circularly polarized beam, the strategy is to evaluate the hot spot size with single spatial frequency ranging from zero to maximum. The minimum spot size is taken as the super-oscillation criterion (SOC). The mathematical description of supercritical criterion, under illumination of circularly polarized plane beam with high NA, is given in detail in the Supplementary Materials (see Supercritical region criterion with eqs. S14 and S15). Typically, the range of RC to SOC can be defined as the supercritical region (see the Supplementary Materials and fig. S1). The focal spot certainly can be further reduced when the light in the main-spot region oscillates faster than the single frequency with minimum spot size. This is termed super-oscillation in mathematics. However, the cost is that the side-lobe intensity will increase exponentially, and the depth of focus is extremely short, which renders real applications of the super-oscillation spot challenging, although it holds promise for an infinitesimal main spot.

From the above analysis, it is found that lateral subdiffraction focal spot with suppressed longitudinal side lobes can be achieved when the lateral optimization target is set in the supercritical region and longitudinal side lobes below an acceptable level (see Optimization on lateral supercritical design and axial side lobes suppression in the Supplementary Materials).

SUPPLEMENTARY MATERIALS

Supplementary material for this article is available at <http://advances.sciencemag.org/cgi/content/full/3/10/e1701398/DC1>

Supplementary Text

fig. S1. The lateral spot size as a function of NA under a circularly polarized light illumination.

fig. S2. The logo of NUS in the focal region.

table S1. Optimized parameters (α_i and C_i) for supercritical MS generation.

table S2. Performance comparison: CPU computing versus GPU parallel computing. References (47–50)

REFERENCES AND NOTES

- H. J. Richter, R. M. Brockie, J. L. Pressesky, Linear density dependence of thermal decay in longitudinal recording. *IEEE Trans. Magn.* **38**, 260–270 (2002).
- D. Weller, M. F. Doerner, Extremely high-density longitudinal magnetic recording media. *Annu. Rev. Mater. Sci.* **30**, 611–644 (2000).
- G. A. Bertero, S. Malhotra, B. Bian, J. Tsoi, M. Avenell, D. Wachenschwanz, T. Yamashita, Longitudinal magnetic media designs for 60–200-Gb/in/sup 2/recording. *IEEE Trans. Magn.* **39**, 651–656 (2003).
- S. N. Piramanayagam, Perpendicular recording media for hard disk drives. *J. Appl. Phys.* **102**, 011301 (2007).
- W. A. Challener, C. Peng, A. V. Itagi, D. Karns, W. Peng, Y. Peng, X. Yang, X. Zhu, N. J. Gokemeijer, Y.-T. Hsia, G. Ju, R. E. Rottmayer, M. A. Seigler, E. C. Gage, Heat-assisted magnetic recording by a near-field transducer with efficient optical energy transfer. *Nat. Photonics* **3**, 220–224 (2009).
- M. A. Seigler, W. A. Challener, E. Gage, N. Gokemeijer, G. Ju, B. Lu, K. Pelhos, C. Peng, R. E. Rottmayer, X. Yang, H. Zhou, T. Rausch, Integrated heat assisted magnetic recording head: Design and recording demonstration. *IEEE Trans. Magn.* **44**, 119–124 (2008).
- N. J. Gokemeijer, H. Zhou, D. Karns, S. Batra, M. Mallary, T. McDaniel, M. Seigler, G. Ju, Y. Peng, M. Xiao, E. Gage, Effect of gradient alignment in heat assisted magnetic recording. *J. Appl. Phys.* **105**, 07B905 (2009).
- L. Zhang, Y. K. Takahashi, A. Perumal, K. Hono, L_{10} -ordered high coercivity (FePt)Ag–C granular thin films for perpendicular recording. *J. Magn. Mater.* **322**, 2658–2664 (2010).
- B. D. Terris, T. Thomson, G. Hu, Patterned media for future magnetic data storage. *Microsyst. Technol.* **13**, 189–196 (2006).
- C. Vogler, C. Abert, F. Bruckner, D. Suess, D. Praetorius, Heat-assisted magnetic recording of bit-patterned media beyond 10 Tb/in². *Appl. Phys. Lett.* **108**, 102406 (2016).
- R. E. Fontana Jr., G. M. Decad, S. R. Hertzler, Volumetric density trends (TB/in.³) for storage components: TAPE, hard disk drives, NAND, and Blu-ray. *J. Appl. Phys.* **117**, 17E301 (2015).
- R. S. Mezrich, Reconstruction effects in magnetic holography. *IEEE Trans. Magn.* **6**, 537–541 (1970).
- R. S. Mezrich, Magnetic holography. *Appl. Opt.* **9**, 2275–2279 (1970).
- M. Tanaka, T. Ito, Y. Nishimura, Diffraction efficiency of magnetic hologram. *IEEE Trans. Magn.* **8**, 523–525 (1972).
- D. Chen, G. Otto, F. Schmit, MnBi films for magneto-optical recording. *IEEE Trans. Magn.* **9**, 66–83 (1973).
- Y. Nakamura, H. Takagi, P. B. Lim, M. Inoue, Magnetic volumetric hologram memory with magnetic garnet. *Opt. Express* **22**, 16439–16444 (2014).
- B. Hillebrands, K. Ounadjela, *Spin Dynamics in Confined Magnetic Structures I. Topics in Applied Physics* (Springer, 2002).
- C. D. Stanciu, F. Hansteen, A. V. Kimel, A. Kirilyuk, A. Tsukamoto, A. Itoh, T. Rasing, All-optical magnetic recording with circularly polarized light. *Phys. Rev. Lett.* **99**, 047601 (2007).
- A. R. Khorsand, M. Savoini, A. Kirilyuk, A. V. Kimel, A. Tsukamoto, A. Itoh, T. Rasing, Role of magnetic circular dichroism in all-optical magnetic recording. *Phys. Rev. Lett.* **108**, 127205 (2012).
- S. Mangin, M. Gottwald, C.-H. Lambert, D. Steil, V. Uhliř, L. Pang, M. Hehn, S. Alebrand, M. Cinchetti, G. Malinowski, Y. Fainman, M. Aeschlimann, E. E. Fullerton, Engineered materials for all-optical helicity-dependent magnetic switching. *Nat. Mater.* **13**, 286–292 (2014).
- Y. Zhang, J. Bai, High-density all-optical magnetic recording using a high-NA lens illuminated by circularly polarized pulse light. *Phys. Lett. A* **372**, 6294–6297 (2008).
- A. V. Kimel, A. Kirilyuk, P. A. Usachev, R. V. Pisarev, A. M. Balbashov, T. Rasing, Ultrafast non-thermal control of magnetization by instantaneous photomagnetic pulses. *Nature* **435**, 655–657 (2005).
- S. Wang, X. Li, J. Zhou, M. Gu, All-optically configuring the inverse Faraday effect for nanoscale perpendicular magnetic recording. *Opt. Express* **23**, 13530–13536 (2015).
- Y. Jiang, X. Li, M. Gu, Generation of sub-diffraction-limited pure longitudinal magnetization by the inverse Faraday effect by tightly focusing an azimuthally polarized vortex beam. *Opt. Lett.* **38**, 2957–2960 (2013).
- P. S. Pershan, J. P. van der Ziel, L. D. Malmstrom, Optically induced magnetization resulting from the inverse Faraday effect. *Phys. Rev. Lett.* **15**, 190–193 (1965).
- Z. Nie, W. Ding, D. Li, X. Zhang, Y. Wang, Y. Song, Spherical and sub-wavelength longitudinal magnetization generated by 4π tightly focusing radially polarized vortex beams. *Opt. Express* **23**, 690–701 (2015).
- S. H. Charap, P.-L. Lu, Y. He, Thermal stability of recorded information at high densities. *IEEE Trans. Magn.* **33**, 978–983 (1997).
- M. Ding, S. J. Poon, Amorphous GdFeCo films exhibiting large and tunable perpendicular magnetic anisotropy. *J. Magn. Mater.* **339**, 51 (2013).
- S. Yoshino, S. Tsunashima, M. Masuda, S. Uchiyama, Magnetostriction and perpendicular magnetic anisotropy of amorphous GdFeCo thin films. *Jpn. J. Appl. Phys.* **27**, 1247 (1988).
- H. Ren, H. Lin, X. Li, M. Gu, Three-dimensional parallel recording with a Debye diffraction-limited and aberration-free volumetric multifocal array. *Opt. Lett.* **39**, 1621–1624 (2014).
- T. Mu, Z. Chen, R. Wu, S. Pacheco, C. Zhang, R. Liang, Generation of a controllable multifocal array from a modulated azimuthally polarized beam. *Opt. Lett.* **41**, 261–264 (2016).
- Z. Nie, W. Ding, G. Shi, D. Li, X. Zhang, Y. Wang, Y. Song, Achievement and steering of light-induced sub-wavelength longitudinal magnetization chain. *Opt. Express* **23**, 21296–21305 (2015).
- M. S. Grinolds, M. Warner, K. De Greve, Y. Dovzhenko, L. Thiel, R. L. Walsworth, S. Hong, P. Maletinsky, A. Yacoby, Subnanometre resolution in three-dimensional magnetic resonance imaging of individual dark spins. *Nat. Nanotechnol.* **9**, 279–284 (2014).
- S. Manz, M. Matsubara, T. Lottermoser, J. Büchi, A. Iyama, T. Kimura, D. Meier, M. Fiebig, Reversible optical switching of antiferromagnetism in TbMnO₃. *Nat. Photonics* **10**, 653–656 (2016).
- T. Higuchi, M. Kuwata-Gonokami, Control of antiferromagnetic domain distribution via polarization-dependent optical annealing. *Nat. Commun.* **7**, 10720 (2016).
- C. J. R. Sheppard, Polarized focused vortex beams: Half-order phase vortices. *Opt. Express* **22**, 18128–18141 (2014).
- G. H. Yuan, S. B. Wei, X.-C. Yuan, Nondiffracting transversally polarized beam. *Opt. Lett.* **36**, 3479–3481 (2011).
- F. Qin, K. Huang, J. Wu, J. Jiao, X. Luo, C. Qiu, M. Hong, Shaping a subwavelength needle with ultra-long focal length by focusing azimuthally polarized light. *Sci. Rep.* **5**, 9977 (2015).
- N. Bokor, N. Davidson, Toward a spherical spot distribution with 4π focusing of radially polarized light. *Opt. Lett.* **29**, 1968–1970 (2004).
- W. Chen, Q. Zhan, Creating a spherical focal spot with spatially modulated radial polarization in 4Pi microscopy. *Opt. Lett.* **34**, 2444–2446 (2009).
- Y. Yu, Q. Zhan, Creation of identical multiple focal spots with prescribed axial distribution. *Sci. Rep.* **5**, 14673 (2015).
- E. Wolf, Electromagnetic diffraction in optical systems. I. An integral representation of the image field. *Proc. R. Soc. London Ser. A* **253**, 349–357 (1959).
- R. Hertel, Theory of the inverse Faraday effect in metals. *J. Magn. Mater.* **303**, L1–L4 (2006).
- L. Novotny, B. Hecht, *Principles of Nano-Optics* (Cambridge Univ. Press, 2006).
- K. Huang, H. Ye, J. Teng, S. P. Ye, B. Luk'yanchuk, C.-W. Qiu, Optimization-free superoscillatory lens using phase and amplitude masks. *Laser Photonics Rev.* **8**, 152–157 (2014).
- F. Qin, K. Huang, J. Wu, J. Teng, C.-W. Qiu, M. Hong, A supercritical lens optical label-free microscopy: Sub-diffraction resolution and ultra-long working distance. *Adv. Mater.* **29**, 1602721 (2017).
- S. Hell, E. H. K. Stelzer, Properties of a 4Pi confocal fluorescence microscope. *J. Opt. Soc. Am. A* **9**, 2159–2166 (1992).
- M. Leutenegger, R. Rao, R. A. Leitgeb, Fast focus field calculations. *Opt. Express* **14**, 11277–11291 (2006).
- M. Zimmerley, P. Mahou, D. Débarre, M.-C. Schanne-Klein, E. Beaurepaire, Probing ordered lipid assemblies with polarized third-harmonic-generation microscopy. *Phys. Rev. X* **3**, 011002 (2013).
- Z.-Q. Nie, H. Lin, X.-F. Liu, A.-P. Zhai, Y.-T. Tian, W.-J. Wang, D.-Y. Li, W.-Q. Ding, X.-R. Zhang, Y.-L. Song, B.-H. Jia, Three-dimensional super-resolution longitudinal magnetization spot arrays. *Light Sci. Appl.* **6**, e17032 (2017).

Acknowledgments: We thank C. S. Bhatia and T. Dutta for the helpful discussions and suggestions. **Funding:** This research is supported by the National Research Foundation, Prime Minister's Office, Singapore, under its Competitive Research Programme (CRP award no. NRF-CRP15-2015-03). Z.N. acknowledges the National Natural Science Foundation of China (no. 11604236) and the Youth Foundation of the Taiyuan University of Technology (no. 2015QN066). B.L. is thankful for the support of the DSI core fund and A*STAR (Agency for Science, Technology and Research) Science and Engineering Research Council (SERC) Pharos (grant 1527000025) and also acknowledges support by the Russian Ministry of Education and Science (#14.W03.31.0008). H.L. acknowledges support from the A*STAR SERC X-ray Photonics Programme (grant no. 1426500049). **Author contributions:** C.H. and C.-W.Q. conceived the idea. C.H., Z.N., and H.Y. conducted the

numerical simulations and contributed to the physical interpretations. C.H., Z.N., H.Y., H.L., X.Y., Y.Z., C.Y., and C.-W.Q. prepared the manuscript. Y.L., R.F., F.W., J.T., and B.L. contributed to the manuscript editing, discussion, and writing. C.-W.Q. supervised the project. All the authors discussed and analyzed the results. **Competing interests:** The authors declare that they have no competing interests. **Data and materials availability:** All data needed to evaluate the conclusions in the paper are present in the paper and/or the Supplementary Materials. Additional data related to this paper may be requested from the authors. All data and analysis details presented in this work are available upon request to C.-W.Q.

Submitted 30 April 2017

Accepted 19 September 2017

Published 13 October 2017

10.1126/sciadv.1701398

Citation: C. Hao, Z. Nie, H. Ye, H. Li, Y. Luo, R. Feng, X. Yu, F. Wen, Y. Zhang, C. Yu, J. Teng, B. Luk'yanchuk, C.-W. Qiu, Three-dimensional supercritical resolved light-induced magnetic holography. *Sci. Adv.* **3**, e1701398 (2017).

Three-dimensional supercritical resolved light-induced magnetic holography

Chenglong Hao, Zhongquan Nie, Huapeng Ye, Hao Li, Yang Luo, Rui Feng, Xia Yu, Feng Wen, Ying Zhang, Changyuan Yu, Jinghua Teng, Boris Luk'yanchuk and Cheng-Wei Qiu

Sci Adv 3 (10), e1701398.
DOI: 10.1126/sciadv.1701398

ARTICLE TOOLS

<http://advances.sciencemag.org/content/3/10/e1701398>

SUPPLEMENTARY MATERIALS

<http://advances.sciencemag.org/content/suppl/2017/10/06/3.10.e1701398.DC1>

REFERENCES

This article cites 48 articles, 1 of which you can access for free
<http://advances.sciencemag.org/content/3/10/e1701398#BIBL>

PERMISSIONS

<http://www.sciencemag.org/help/reprints-and-permissions>

Use of this article is subject to the [Terms of Service](#)

Science Advances (ISSN 2375-2548) is published by the American Association for the Advancement of Science, 1200 New York Avenue NW, Washington, DC 20005. 2017 © The Authors, some rights reserved; exclusive licensee American Association for the Advancement of Science. No claim to original U.S. Government Works. The title *Science Advances* is a registered trademark of AAAS.

Supplementary Materials for **Three-dimensional supercritical resolved light-induced magnetic holography**

Chenglong Hao, Zhongquan Nie, Huapeng Ye, Hao Li, Yang Luo, Rui Feng, Xia Yu, Feng Wen,
Ying Zhang, Changyuan Yu, Jinghua Teng, Boris Luk'yanchuk, Cheng-Wei Qiu

Published 13 October 2017, *Sci. Adv.* **3**, e1701398 (2017)
DOI: 10.1126/sciadv.1701398

This PDF file includes:

- Supplementary Text
- fig. S1. The lateral spot size as a function of NA under a circularly polarized light illumination.
- fig. S2. The logo of NUS in the focal region.
- table S1. Optimized parameters (α_i and C_i) for supercritical MS generation.
- table S2. Performance comparison: CPU computing versus GPU parallel computing.
- References (47–50)

Supplementary Text

Theoretical model for 4π microscopy and beams combination method

Before exploration of light-induced magnetization in the 4π beams combination configuration, it is prerequisite to investigate the relevant electric field distributions of a single high-NA objective. In principle, the effect of polarization should be taken into account in the high-NA geometry. When a linearly x -polarized plane wave illuminates an aplanatic lens, the electric fields \mathbf{E} in the vicinity of the focus can be expressed according to Richards and Wolf (42) as

$$\mathbf{E}(r, \varphi, z) = \begin{bmatrix} e_x \\ e_y \\ e_z \end{bmatrix} = \begin{bmatrix} -iA(I_0 + I_2 \cos 2\varphi) \\ -iAI_2 \sin 2\varphi \\ -2AI_1 \cos \varphi \end{bmatrix} \quad (\text{S1})$$

with

$$I_0 = \int_0^\alpha P(\theta)(1 + \cos \theta) \sin \theta J_0(kr \sin \theta) e^{ikz \cos \theta} d\theta \quad (\text{S2a})$$

$$I_1 = \int_0^\alpha P(\theta) \sin^2 \theta J_1(kr \sin \theta) e^{ikz \cos \theta} d\theta \quad (\text{S2b})$$

$$I_2 = \int_0^\alpha P(\theta)(1 - \cos \theta) \sin \theta J_2(kr \sin \theta) e^{ikz \cos \theta} d\theta \quad (\text{S2c})$$

where A is the field amplitude distribution at the pupil plane, α denotes the convergence semi-angle of the objective, $P(\theta)$ is the pupil apodization function, which is equal to $\cos^{1/2} \theta$ for the objective obeying the Abbe condition, J_n is the n^{th} -order Bessel function of the first kind, $k = 2\pi/\lambda$ is the wave vector in image space. (r, φ, z) are cylindrical coordinates centered at the focus. Similarly, for a linearly y -polarized plane wave illumination, the electric fields \mathbf{E}' in the vicinity of the focus can be expressed as

$$\mathbf{E}'(r, \varphi, z) = \begin{bmatrix} e'_x \\ e'_y \\ e'_z \end{bmatrix} = \begin{bmatrix} -iAI_2 \sin 2\varphi \\ -iA(I_0 - I_2 \cos 2\varphi) \\ -2AI_1 \sin \varphi \end{bmatrix} \quad (\text{S3})$$

For a circularly polarized light, the Jones vector is expressed as

$$\mathbf{J} = \begin{bmatrix} \pm i \\ 1 \end{bmatrix} \quad (\text{S4})$$

where the + and – signs are corresponding to the left- and right-handed circular polarization, respectively. The circularly polarized light can be considered as the superposition of two orthogonally linearly polarized beams with $\pi/2$ phase retardation between them. Therefore, the electric field in the focus under left-handed circularly polarized incidence is obtained as

$$\mathbf{E}_{\text{circ}}^{\text{L}}(r, \varphi, z) = \begin{bmatrix} ie_x + e'_x \\ ie_y + e'_y \\ ie_z + e'_z \end{bmatrix} = \begin{bmatrix} A(I_0 + I_2 e^{-i2\varphi}) \\ -iA(I_0 - I_2 e^{-i2\varphi}) \\ -2AI_1 e^{-i\varphi} \end{bmatrix} \quad (\text{S5})$$

For the right-handed circularly polarized incidence we have

$$\mathbf{E}_{\text{circ}}^{\text{R}}(r, \varphi, z) = \begin{bmatrix} -ie_x + e'_x \\ -ie_y + e'_y \\ -ie_z + e'_z \end{bmatrix} = \begin{bmatrix} -A(I_0 + I_2 e^{i2\varphi}) \\ -iA(I_0 - I_2 e^{i2\varphi}) \\ 2iAI_1 e^{i\varphi} \end{bmatrix} \quad (\text{S6})$$

To transform these electric-field components along the Cartesian-coordinate axes into their cylindrical-coordinate counterparts, we need to employ the following equation

$$\begin{bmatrix} E_r \\ E_\varphi \end{bmatrix} = \begin{bmatrix} \cos \varphi & \sin \varphi \\ -\sin \varphi & \cos \varphi \end{bmatrix} \begin{bmatrix} E_x \\ E_y \end{bmatrix} \quad (\text{S7})$$

The electric fields in the vicinity of the focus of left-handed and right-handed circularly polarized light in cylindrical coordinate are

$$\mathbf{E}_{\text{circ}}^{\text{L}}(r, \varphi, z) = \begin{bmatrix} E_r(r, \varphi, z) \\ E_\varphi(r, \varphi, z) \\ E_z(r, \varphi, z) \end{bmatrix} = Ae^{-i\varphi} \begin{bmatrix} (I_0 + I_2) \\ -i(I_0 - I_2) \\ -2iI_1 \end{bmatrix} \quad (\text{S8a})$$

and

$$\mathbf{E}_{\text{circ}}^{\text{R}}(r, \varphi, z) = \begin{bmatrix} E_r(r, \varphi, z) \\ E_\varphi(r, \varphi, z) \\ E_z(r, \varphi, z) \end{bmatrix} = A e^{i\varphi} \begin{bmatrix} -(I_0 + I_2) \\ -i(I_0 - I_2) \\ 2iI_1 \end{bmatrix} \quad (\text{S8b})$$

Essentially, the key to garner purely longitudinal magnetization all-optically in the magnetic hologram is to remove electric field along axial direction (\mathbf{E}_z). The 4π microscopic system is preferred due to its fascinating capability in achieving axial super-resolution simultaneously (26, 39–41). In the 4π microscopic system, the electric fields near the foci are the superposition of the fields from two counter-propagating focused beams, which is (47)

$$\mathbf{E}_f(r, \varphi, z) = \mathbf{E}(r, \varphi, z) + \mathbf{E}(r, \varphi, -z) \quad (\text{S9})$$

To achieve both perfect destructive interference of the axial electric field and constructive interference of the transverse counterpart at the focal plane, so as to make the pure transversally polarized optical field with sub-diffraction spot size possible, as well as inducing pure longitudinal magnetization via the inverse Faraday effect simultaneously, we propose 4π beams combination microscopic system. Therefore, the electric fields near foci are superposition of the multi-beams fields, shown in Fig. 1(a) in main text. That is

$$\mathbf{E}_i(r, \varphi, z) = \sum_{i=1}^6 C_i [\mathbf{E}_i(r, \varphi, z) + \mathbf{E}_i(r, \varphi, -z)] \quad (\text{S10})$$

where \mathbf{E}_i stands for the focal electric fields with semi-aperture α_i . C_i denotes the amplitude modulation coefficient for corresponding beam. $-z$ in \mathbf{E}_i indicates that the field is counter-propagating. In this article, the optimal semi-apertures and corresponding amplitude modulation coefficients are obtained through optimization.

Substituting Equation S8a into Equation S10, we obtain the electric field in the focal vicinity of this 4π beams combination microscopic system with left-handed circularly polarized plane wave illumination as

$$\mathbf{E}_t^{\text{LC}}(r, \varphi, z) = \begin{bmatrix} E_r(r, \varphi, z) \\ E_\varphi(r, \varphi, z) \\ E_z(r, \varphi, z) \end{bmatrix} = A e^{-i\varphi} \begin{bmatrix} (H_0 + H_2) \\ -i(H_0 - H_2) \\ -2iH_1 \end{bmatrix} \quad (\text{S11})$$

Similarly, substituting Equation S8b into Equation S10, we obtain the electric field in the focal vicinity of this 4π beams combination microscopic system with right-handed circularly polarized plane wave illumination as

$$\mathbf{E}_t^{\text{RC}}(r, \varphi, z) = \begin{bmatrix} E_r(r, \varphi, z) \\ E_\varphi(r, \varphi, z) \\ E_z(r, \varphi, z) \end{bmatrix} = A e^{i\varphi} \begin{bmatrix} -(H_0 + H_2) \\ -i(H_0 - H_2) \\ 2iH_1 \end{bmatrix} \quad (\text{S12})$$

with H_i ($i=0, 1, \text{ and } 2$) are three integrals of

$$H_0 = \sum C_i \int_0^{\alpha_i} 2 \cos^{\frac{1}{2}} \theta \cos(kz \cos \theta) \sin \theta (1 + \cos \theta) J_0(kr \sin \theta) d\theta \quad (\text{S13a})$$

$$H_1 = \sum C_i \int_0^{\alpha_i} 2 \cos^{\frac{1}{2}} \theta \cos(kz \cos \theta) \sin^2 \theta J_1(kr \sin \theta) d\theta \quad (\text{S13b})$$

$$H_2 = \sum C_i \int_0^{\alpha_i} 2 \cos^{\frac{1}{2}} \theta \cos(kz \cos \theta) \sin \theta (1 - \cos \theta) J_2(kr \sin \theta) d\theta \quad (\text{S13c})$$

Supercritical region criterion

For a spherical-lens-based optical imaging system, the light is usually focused into an Airy spot with the size of $0.61\lambda/NA$, accompanied by a very weak side lobe with a mere 1.75% intensity of main spot (44). Sub-diffraction limit focusing is feasible at the cost of increasing energy in the side lobes. For non-polarized incident light, higher spatial frequency corresponds to a smaller spot. The extreme case is that light with only the maximum spatial frequency is focused into a hotspot with intensity profile proportional to $|J_0(krNA)|^2$, which is named as “maximum-frequency spot”. This maximum-frequency spot has a main lobe of $0.38\lambda/NA$ and comes with moderate side lobes (16.2% of main spot) (45, 46). Following the same strategy, we examine the spot size that corresponds to single frequency with circularly polarized incident light. The minimum lateral spot size when the single frequency traverses from 0 to semi-aperture α , is taken as the super-oscillation criterion (SOC). The range of RC

to SOC can be defined as supercritical region. The mathematical description of SOC can be expressed as

$$\begin{aligned}
& \text{Min FWHM}(I(\theta)) \\
& \text{s.t. } \theta \in [0, \alpha], \\
& I = I_0'^2 + 2I_1'^2 + I_2'^2
\end{aligned} \tag{S14}$$

with

$$I_0' = \cos^{\frac{1}{2}} \theta \sin \theta (1 + \cos \theta) J_0(kr \sin \theta) \tag{S15a}$$

$$I_1' = \cos^{\frac{1}{2}} \theta \sin^2 \theta J_1(kr \sin \theta) \tag{S15b}$$

$$I_2' = \cos^{\frac{1}{2}} \theta \sin \theta (1 - \cos \theta) J_2(kr \sin \theta) \tag{S15c}$$

where α is the semi-aperture of objective. The $\text{FWHM}(I(\theta))$ denotes the function which is employed to find the spot size at full width at half maximum. Figure S1 shows the resulted RC and SOC in our 4π system with oil-immersed objective ($NA=1.43$, $NA = 1.509 \times 0.95$). The SOC has a similar shape like the RC. For a given NA, the spot with size below the diffraction limit and above SOC can be called supercritical spot. What's more, the SOC for circularly polarized light is quite close to the SOC for non-polarized light when $\sin \alpha < 0.6$. The SOC is 0.3512λ and RC is 0.4255λ in our case ($NA = 1.509 \times 0.95$), thus, the resultant supercritical region is between 0.3512λ to 0.4255λ . This finely distinguished roadmap provides an instructive guide that supercritical region is the best choice when one pursues a super-resolution spot without high side lobes outside designed region. More importantly, this calculation method can be extended to incident light with other polarization modes, which provides a routine to find the SOC for different incident light.

Optimization on lateral supercritical design and axial side lobes suppression

The optimization target in our calculation is to minimize spot volume with following constrains. First, the minimum and maximum NA in beams combination is 0.981 ($\sin \alpha = 0.65$) and 1.434 ($\sin \alpha = 0.95$), respectively. Second, the lateral spot size is set to be in the supercritical region. Last, the side lobes should be below 30% of main spot, which is practical for real-life application. The optimization is implemented by using interior point

optimization algorithm, considering the beam sizes of six incident circularly polarized light and corresponding amplitude coefficients as optimizing parameters. The optimized parameters are shown in table S1.

Theory of light induced magnetization and magnetization reversal

Essentially, we treat conducting electrons within MO medium as a collisionless plasma in which the electrons can migrate freely (25, 43). As a consequence, the effective magnetization, in the isotropic MO material, induced by incident beams in 4π beams combination system reads

$$\mathbf{M}(r, \varphi, z) = i\gamma \mathbf{E}_t \times \mathbf{E}_t^* \quad (\text{S16})$$

where \mathbf{E}_t^* denotes the complex conjugate of \mathbf{E}_t , γ is the magneto-optical susceptibility.

Substituting Equations S11- S13 into Equation S16, and doing some simple mathematical simplifications, the induced magnetization fields by left-handed circularly polarized light and right-handed circularly polarized light in the 4π beams combination system are given by

$$\mathbf{M}_{\text{LC}}(r, \varphi, z) = \begin{bmatrix} M_r(r, \varphi, z) \\ M_\varphi(r, \varphi, z) \\ M_z(r, \varphi, z) \end{bmatrix} = -2i\gamma A^2 \begin{bmatrix} 0 \\ 2(H_0 + H_2)H_1 \\ H_0^2 - H_2^2 \end{bmatrix} \quad (\text{S17a})$$

and

$$\mathbf{M}_{\text{RC}}(r, \varphi, z) = \begin{bmatrix} M_r(r, \varphi, z) \\ M_\varphi(r, \varphi, z) \\ M_z(r, \varphi, z) \end{bmatrix} = 2i\gamma A^2 \begin{bmatrix} 0 \\ -2(H_0 + H_2)H_1 \\ H_0^2 - H_2^2 \end{bmatrix} \quad (\text{S17b})$$

with H_i ($i=0, 1, \text{ and } 2$) in Equation S13.

Apparently, it is found from Equations S13 and S17 that the radial magnetization component disappears absolutely for both light helicity. Moreover, the induced total magnetization field is primarily determined by the longitudinal magnetization components as the value of H_0 always overwhelms that of either H_1 or H_2 in the focal region. Especially, the resultant magnetization field at $r=0$ and $z=0$ becomes totally longitudinal, i.e. $\mathbf{M}=\mathbf{M}_z$, which is essentially different from the magnetization induced by single high-NA objective.

From Equation S17a and Equation S17b, one can immediately conclude that the magnetization direction under left-handed circularly polarized incident light is opposite to that under right-handed circularly polarized incident light at focal region at $r=0$ and $z=0$, i.e. $\mathbf{M}_{LC} = -\mathbf{M}_{RC}$. This theoretically proves that the magnetization reversal occurs via two illuminations with opposite light helicity (18).

Theoretical model for multifoci by multiple phase filters

To obtain desired multifoci pattern analytically, a common used routine is to convert the vectorial diffraction integral of Equations S1 and S2 into Fourier transform field $\mathbf{E}_0(x, y, z)$ (48, 49). Thus, considering the incident beams modulated by multiple phase filters and following our previous analysis in (50), the focal distribution in Equation S1 can be rewritten as

$$\begin{aligned}\mathbf{E}(x, y, z) &= \iint [t(x, y) \mathbf{E}_0(x, y, z)] \exp[-i(k_x x + k_y y)] dk_x dk_y \\ &= FT\{t(x, y)\} * FT\{\mathbf{E}_0(x, y, z)\}\end{aligned}\quad (\text{S18})$$

where $t(x, y)$ is the transmittance function of MPFs, $FT\{\}$ denotes the Fourier transform, the symbol $*$ represents the convolution operation, and $\mathbf{E}_0(x, y, z)$ describes the weighted field with a vector angular spectrum form, which is

$$\mathbf{E}_0(x, y, z) = (\mathbf{e}_x + i\mathbf{e}_y) \exp(ik_z z) / \cos \theta \quad (\text{S19})$$

where \mathbf{e}_x and \mathbf{e}_y are unit vectors in the x and y directions at the back aperture plane, respectively. $\mathbf{k} = (k_x, k_y, k_z)$ is the wave vector. As can be seen from Equation S18, the distribution of the focused field is represented as a spatial convolution with Fourier transform of $t(x, y)$ and Fourier transform of $\mathbf{E}_0(x, y, z)$. This implies that it is feasible to focus light into multifocal spots provided that Fourier transform of $t(x, y)$ exhibits a multifocal function. In a similar fashion, the super-resolved magnetization spot array can be generated by focusing circularly polarized light beams impinging on the proposed multiple phase filters. To this end, the following analytical formula is given as

$$t(x, y) = \sum_{i=1}^N \exp[-ik(a_i x + b_i y)] \times \exp(-ikc_i \cos \theta) \quad (\text{S20})$$

where N is an integer, giving the total number of spots along the x , y and z directions; a_i , b_i and c_i represent the displacements along x , y and z directions, respectively. Combining Equations S16, S17 and Equations S18 to S20, the multifoci magnetization spots can be produced by focusing left-handed circularly polarized plane beam imposed by the multiple phase filters, which is shown in Fig. 3 and Fig. 2.

GPU parallel computing

When the multifocal off-axial magnetization spots are numerically generated, it includes time-consuming double integral in Debye vectorial diffraction theory. Calculation based on Fast Fourier Transform was proposed to accelerate the computing speed. However, the results from this method are accurate only under the given sampling conditions. Therefore, another route, which is more general and fast compared with normal calculation, is desired. Here, we propose to use GPU parallel computing to accelerate computing speed of the double integral. The double integral is programmed with GPU array and parallel computing on the platform of Matlab 2016a (www.mathworks.com/videos/parallel-computing-tutorial-gpu-computing-with-matlab-9-of-9-91572.html). The computing speed is accelerated by ~ 15 times compared with CPU computing. The performances of GPU parallel computing vs. CPU computing are listed in the table S2. From table S2, the conclusion can be drawn that GPU parallel computing greatly accelerate calculation speed to ~ 15 times, which can potentially be a new routine for massive calculation.

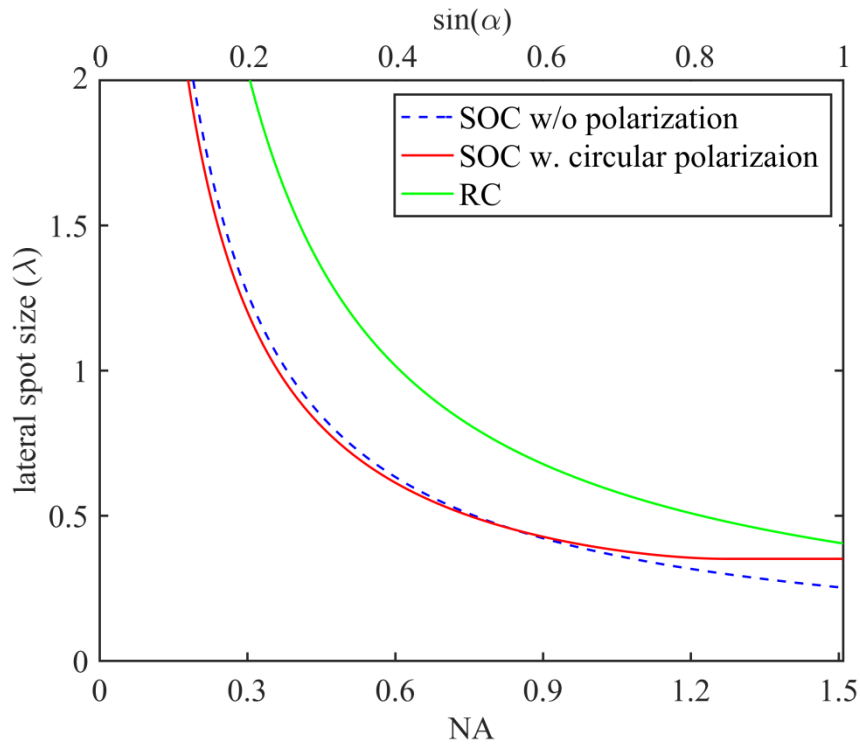


fig. S1. The lateral spot size as a function of NA under a circularly polarized light illumination. The red curve indicates the super-oscillation criterion (SOC). The green curve indicates the Rayleigh Criterion (RC). The region below SOC is super-oscillation, the region between red curve and green curve is supercritical region under circularly polarized light illumination. The blue dash line indicates the SOC for non-polarized light. The difference between SOC for circularly polarized light and SOC for non-polarized light is relative small when NA is less than 0.9 ($\sin \alpha < 0.6$).

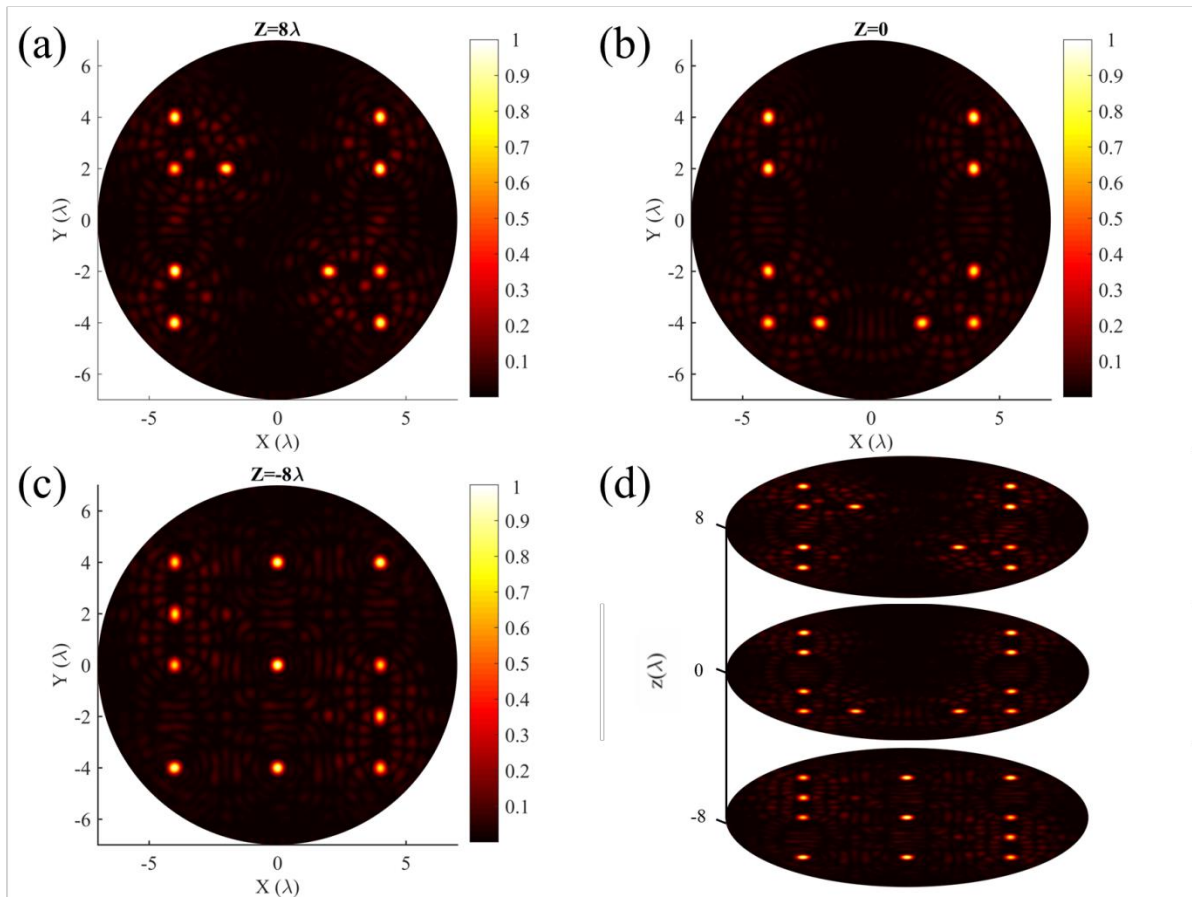


fig. S2. The logo of NUS in the focal region. (a) The capital letter “N” in XY plane at $Z=8\lambda$ with 10 MSs; (b) The capital letter “U” in XY plane at $Z=0$ with 10 MSs; (c) The capital letter “S” in XY plane at $Z=-8\lambda$ with 11 MSs; (d) The 3D slice of logo NUS in the focal region.

table S1. Optimized parameters (α_i and C_i) for supercritical MS generation.

| | 1 | 2 | 3 | 4 | 5 | 6 |
|---|---------|--------|---------|--------|--------|---------|
| Aperture (α_i rad) | 0.6546 | 0.6819 | 0.7002 | 0.7617 | 0.7795 | 0.9452 |
| Amplitude modulation coefficients (C_i) | -0.4843 | 0.1292 | -0.4000 | 0.7541 | 0.6152 | -1.0000 |

table S2. Performance comparison: CPU computing versus GPU parallel computing.

| | Pyramid (5 spots, calculating at Plane ABCD) | NUS logo (31 spots calculation at “N” plane) | NUS logo (31 spots calculation at “U” plane) | NUS logo (31 spots calculation at “S” plane) |
|---|---|---|---|---|
| Calculation time (hour): CPU: i7-6700 8M Cache, @3.4 GHz up to 4.00 GHz, with 16G RAM | 25.75 | 152.46 | 142.38 | 160.2 |
| Calculation time (hour):GPU: Geforce GTX 1070 1920 cores @1.5GHz, with 8GB RAM | 1.79 (14.4 ^x speed increase) | 10.03 (15.2 ^x speed increase) | 9.62 (14.8 ^x speed increase) | 10.68 (15.0 ^x speed increase) |